

FINITE AMPLITUDE STEADY-STATE ONE-DIMENSIONAL WAVES IN FLUIDIZED BEDS*

YURI D. SOBRAL[†] AND E. JOHN HINCH[‡]

Abstract. In this work, we investigate one-dimensional concentration instabilities that occur in fluidized beds. We use the averaged equations of motion for fluidized beds and use closure relations for the stress tensors available in the literature. A linear stability analysis is carried out in order to characterize the frequency, the propagation velocity, and the growth rates of small amplitude disturbances. A fully nonlinear transient numerical solution of the governing equations is also obtained. The linear and nonlinear growth and saturation of concentration waves as they saturate, i.e., as they reach a finite amplitude steady-state, is explored. The one-dimensional governing PDEs are recast into a nonlinear ODE in the frame of reference moving with the velocity of the saturated waves. We propose a numerical method to solve this eigenvalue problem, the result of which leads to the concentration profile, the wavelength, and the propagation velocity of the saturated waves. The results are compared with the predictions of the linear theory, with the fully nonlinear transient numerical simulations, and with the experimental data available. We explore some of the limits of validity of the linear theory and of the closure models.

Key words. fluidized beds, concentration waves, saturated waves, linear stability, eigenvalue problem

AMS subject classifications. 76E99, 76T99, 76D33

DOI. 10.1137/16M1084031

1. Introduction. Consider the flow of a fluid through a set of solid particles. The particles are supported by a perforated plate, and the flow is in the upward direction. When the flow rate is small, the fluid flows through the set of particles as if it was a porous medium. If the flow rate is increased to a level at which the drag exerted on the particles by the fluid balances their weight corrected for buoyancy, then some particles become mobile and a very small expansion of the region occupied by the particles is observed. Any further increase on the flow rate would cause the particles to become fully mobile and to occupy a larger region of the reservoir. At this stage, the particles are said to be fluidized, and the system is usually referred to as a fluidized bed. The name fluidized bed is due to the fact that the particles in this condition can be stirred and poured as a fluid [1, 2].

Fluidized beds are unstable, and in actual devices the propagation of regions of very low concentration of particles, called bubbles, are commonly observed [1]. There have been several studies on this unstable nature [1, 2], and most of them tried to connect the instability of plane wave perturbations of the homogeneous state of fluidization to the formation of bubbles [1, 2, 3, 4]. However, the natural evolution of plane wave perturbation confined to one-dimensional systems is itself an interesting problem of nonlinear wave evolution, having received the attention of several theoretical [5, 6], numerical [3, 7], and experimental [8] investigations.

*Received by the editors July 19, 2016; accepted for publication (in revised form) December 5, 2016; published electronically February 8, 2017.

<http://www.siam.org/journals/siap/77-1/M108403.html>

Funding: This work was supported by Fundação Coordenação de Aperfeiçoamento de Pessoal de Nível Superior (CAPES), Ministério da Educação, Brazil.

[†]Departamento de Matemática, Universidade de Brasília. Campus Universitário Darcy Ribeiro, 70910-900 Brasília-DF, Brazil (ydsobral@unb.br).

[‡]Department of Applied Mathematics and Theoretical Physics, Centre for Mathematical Sciences, University of Cambridge, Cambridge, CB3 0WA, United Kingdom (E.J.Hinch@damtp.cam.ac.uk).

Following the natural evolution of the subject so far, and mostly inspired by the work of [8], the present study aims to address questions on the evolution of concentration waves, i.e., the one-dimensional limit of instabilities in fluidized beds is fully characterized in this work. We investigate in detail the evolution of small amplitude linear instabilities into finite amplitude waves and characterize the steady-state that is reached at this stage, herein referred to as the saturated wave regime. The theory proposed to describe the saturated regime in [8], which was their major rheological tool to characterize the particulate phase, is then explored analytically and numerically, and the influence of physical parameters of the system is evaluated in detail. In addition, some aspects of the new constitutive equations proposed from the experiments in [8] are also briefly discussed.

2. Formulation of the problem. The governing equations used in this work are those derived originally in [9] and more recently used in [3, 10]. We assume that both the fluid and the fluidized particles are isothermal continua that interpenetrate and interact through a surface without surface tension, so that the dynamics of the flow is described by averaged equations of conservation of mass and momentum [9].

Let \mathbf{u} denote the averaged velocity of the fluid phase and \mathbf{v} that of the particulate phase. The local concentration of particles is ϕ , and ρ stands for density and μ for dynamical viscosity, the subscripts f or p indicating if the physical property refers to the fluid or to the particulate phase, respectively. The continuity equation for the particulate phase and for the fluid phase are written as

$$(2.1) \quad \frac{\partial \phi}{\partial t} + \nabla \cdot (\mathbf{v}\phi) = 0 \quad \text{and} \quad -\frac{\partial \phi}{\partial t} + \nabla \cdot [\mathbf{u}(1 - \phi)] = 0,$$

respectively. The momentum equation for the particulate phase is written as

$$(2.2) \quad \phi \rho_p \left(\frac{\partial \mathbf{v}}{\partial t} + \mathbf{v} \cdot \nabla \mathbf{v} \right) = \nabla \cdot \mathbf{T}_p + \mathbf{f} + \phi(\rho_p - \rho_f) \mathbf{g} + \phi \rho_f \left(\frac{\partial \mathbf{u}}{\partial t} + \mathbf{u} \cdot \nabla \mathbf{u} \right),$$

where the stress tensor of the particulate phase is represented by \mathbf{T}_p and the fluid-particle interaction force is denoted by \mathbf{f} . A similar equation can be written for the fluid phase, that is,

$$(2.3) \quad (1 - \phi) \rho_f \left(\frac{\partial \mathbf{u}}{\partial t} + \mathbf{u} \cdot \nabla \mathbf{u} \right) = \nabla \cdot \mathbf{T}_f - \mathbf{f} + (1 - \phi) \rho_f \mathbf{g},$$

where now \mathbf{T}_f denotes the stress tensor of the fluid phase. The particulate phase stress tensor is defined to be

$$(2.4) \quad \mathbf{T}_p = -p_p(\phi) \mathbf{I} + \mu_p(\phi) \left[\nabla \mathbf{v} + \nabla \mathbf{v}^T - \frac{2}{3} (\nabla \cdot \mathbf{v}) \mathbf{I} \right],$$

where $p_p(\phi)$ denotes the particle-phase pressure and $\mu_p(\phi)$ the particle-phase viscosity, both quantities being functions of the particle concentration. For the fluid phase, one simply writes

$$(2.5) \quad \mathbf{T}_f = -p \mathbf{I} + \mu_f \left[\nabla \mathbf{u} + \nabla \mathbf{u}^T - \frac{2}{3} (\nabla \cdot \mathbf{u}) \mathbf{I} \right],$$

where p is the pressure and μ_f the viscosity of the fluid phase. The fluid-particle interaction force is given by

$$(2.6) \quad \mathbf{f} = \beta(\phi)(\mathbf{u} - \mathbf{v}) + \rho_f \vartheta(\phi) \left[\left(\frac{\partial \mathbf{u}}{\partial t} + \mathbf{u} \cdot \nabla \mathbf{u} \right) - \left(\frac{\partial \mathbf{v}}{\partial t} + \mathbf{v} \cdot \nabla \mathbf{v} \right) \right] + \phi \nabla \cdot \mathbf{T}_f,$$

where the first term denotes a linear viscous drag, the second term is a virtual mass drag, and the third term is a pressure drag [9]. Here, $\beta(\phi)$ is a coefficient that is determined from the Richardson and Zaki correlation ([11] and (2.10) below),

$$(2.7) \quad \beta(\phi) = \frac{(\rho_p - \rho_f)g}{v_t} \frac{\phi}{(1 - \phi)^{n-1}},$$

with v_t denoting the terminal velocity of the particles and with n being an experimental parameter. The added mass coefficient for the particulate phase, despite being dependent on the concentration of particles, is assumed to be identical to that of a single sphere, so that the reduced added mass coefficient $\vartheta(\phi)$ is given by

$$(2.8) \quad \vartheta(\phi) = \frac{1}{2} \frac{1}{1 - \phi}.$$

We now restrict our attention to one-dimensional disturbances. However, before presenting the one-dimensional equations, a few simplifications can be carried out. The first one is that the momentum equation for the fluid phase is not necessary if one seeks the solutions of (2.1) and (2.2) for ϕ , v , and u , where v and u are the one-dimensional representations of \mathbf{v} and \mathbf{u} , respectively. Moreover, by adding and integrating the one-dimensional versions of (2.1), we obtain the mean flow rate in the fluidized bed q ,

$$(2.9) \quad q = \phi v + (1 - \phi)u,$$

that relates the velocity of the fluid and of the particles algebraically. The quantity q is related to the homogeneous concentration in the fluidized bed ϕ_o and the particle terminal velocity by the Richardson and Zaki correlation [11], that is,

$$(2.10) \quad q = v_t(1 - \phi_o)^n.$$

The one-dimensional version of the momentum equation for the particulate phase, (2.2), is written as

$$(2.11) \quad \begin{aligned} & \phi(\rho_p + \vartheta\rho_f) \left(\frac{\partial v}{\partial t} + v \frac{\partial v}{\partial x} \right) - \phi\rho_f(1 + \vartheta) \left(\frac{\partial u}{\partial t} + u \frac{\partial u}{\partial x} \right) + \frac{\partial p_p}{\partial x} \\ & = \frac{4}{3} \frac{\partial}{\partial x} \left(\mu_p \frac{\partial v}{\partial x} \right) + \beta(u - v) - \phi(\rho_p - \rho_f)g. \end{aligned}$$

Finally, the continuity equation for the particulate phase in one-dimension is given by

$$(2.12) \quad \frac{\partial \phi}{\partial t} + \frac{\partial}{\partial x} (v\phi) = 0.$$

3. Linear stability analysis. In this section, we investigate the stability of small amplitude waves propagating along one-dimensional fluidized beds. The results from this section will be used as references in the analyses of the results of the following sections.

The one-dimensional equations (2.11) and (2.12) are linearized around the homogeneous state of fluidization, that is, $\phi = \phi_o + \phi_1$, $u = q/(1 - \phi_o) + u_1$, and $v = v_1$ with ϕ_1 , u_1 , and v_1 being small. Combining the perturbed equations to successively

write terms in u_1 and v_1 in terms of ϕ_1 , we then obtain one single equation in terms of particle concentration disturbances:

$$(3.1) \quad \mathcal{A} \frac{\partial^2 \phi_1}{\partial t^2} - \mathcal{B} \frac{\partial^3 \phi_1}{\partial x^2 \partial t} + \mathcal{C} \frac{\partial^2 \phi_1}{\partial t \partial x} - \mathcal{D} \frac{\partial^2 \phi_1}{\partial x^2} + \mathcal{E} \frac{\partial \phi_1}{\partial x} + \mathcal{F} \frac{\partial \phi_1}{\partial t} = 0.$$

The coefficients in (3.1) are given by

$$(3.2) \quad \begin{aligned} \mathcal{A} &= (\rho_p + \rho_f \vartheta(\phi_o)) + \frac{\phi_o}{1 - \phi_o} \rho_f (1 + \vartheta(\phi_o)), & \mathcal{B} &= \frac{4}{3} \frac{\mu_p(\phi_o)}{\phi_o}, \\ \mathcal{C} &= \frac{2\phi_o \rho_f q}{(1 - \phi_o)^2} (1 + \vartheta(\phi_o)), & \mathcal{D} &= \left. \frac{dp_p}{d\phi} \right|_{\phi_o} - \frac{q^2 \phi_o \rho_f}{(1 - \phi_o)^3} (1 + \vartheta(\phi_o)), \\ \mathcal{E} &= \frac{\beta(\phi_o) q}{(1 - \phi_o)^2} + \frac{q}{1 - \phi_o} \left. \frac{d\beta}{d\phi} \right|_{\phi_o} + (\rho_p - \rho_f) g, & \mathcal{F} &= \frac{\beta(\phi_o)}{\phi_o (1 - \phi_o)}, \end{aligned}$$

and depend on the physical parameters of the fluidized bed and on the concentration of particles at the state of homogeneous fluidization, ϕ_o . Equation (3.1) is the basis of the stability analysis developed in this work.

Imposing plane wave disturbances as $\phi_1 \sim \exp(i(\kappa x - \omega t))$, where κ denotes the wave number and ω the frequency of the disturbances, (3.1) can be rewritten as

$$(3.3) \quad -\mathcal{A}i\omega^2 + \mathcal{B}i\kappa^2\omega + \mathcal{C}\kappa\omega - \mathcal{D}\kappa^2 + \mathcal{E}i\kappa - \mathcal{F}i\omega = 0,$$

from which the dispersion relation of the disturbances can be found.

The first approximation that can be made is to consider initially the case where there are neither inertial effects nor particle-phase pressure effects. This case is obtained by setting to zero in (3.3) the coefficients associated to inertial and particle-phase pressure mechanisms, that is, $\mathcal{A} = \mathcal{C} = \mathcal{D} = 0$. In this case, the dispersion relation is found to be given by

$$(3.4) \quad \omega = \frac{\mathcal{E}\kappa}{\mathcal{F} + \mathcal{B}\kappa^2} = \frac{c_o \kappa}{1 + \ell^2 \kappa^2},$$

where c_o is the kinematic wave speed, defined as

$$(3.5) \quad c_o = \frac{\mathcal{E}}{\mathcal{F}} = v_t n \phi_o (1 - \phi_o)^{n-1},$$

and where the viscous length scale ℓ is defined as

$$(3.6) \quad \ell^2 = \frac{\mathcal{B}}{\mathcal{F}} = \frac{4}{3} \frac{\mu_p(\phi_o)}{\phi_o} \frac{v_t (1 - \phi_o)^n}{g(\rho_p - \rho_f)}.$$

The velocity of disturbances can be determined from the dispersion relation given in (3.4):

$$(3.7) \quad c = \frac{\omega}{\kappa} = \frac{c_o}{1 + \ell^2 \kappa^2}.$$

These results allow us to conclude that the propagation of the waves in fluidized beds is mainly dominated by viscosity, drag, and weight corrected for buoyancy and that, on the absence of inertial and particle-phase pressure mechanisms, there is neither growth nor decay of the disturbances, i.e., there is only propagation of modes with velocities given by (3.7).

However, when the full version of (3.3) is considered and inertial terms are present, a different behavior is observed. There are now two approaches that can be followed to investigate the stability of fluidized beds: a temporal approach, in which the growth rate in time of the amplitudes is determined, or a spatial approach, where the growth rate in space is determined. Because of the convective nature of the instabilities in fluidized beds [12], it is more convenient to investigate the spatial growth of the concentration disturbances rather than their temporal growth. In this case, it is assumed that the wave number is complex, that is, $\kappa = \kappa_r + i\kappa_i$, and the frequency of the disturbances is real. The real part κ_r is the usual wave number, and κ_i is the spatial growth rate of the disturbances. Solving (3.3) for $\kappa = \kappa(\omega)$, we obtain

$$(3.8) \quad \kappa = \frac{-\mathcal{C}\omega - \mathcal{E}i}{\mathcal{D} - \mathcal{B}i\omega} \pm \frac{\sqrt{(\mathcal{C}\omega + \mathcal{E}i)^2 + 4(\mathcal{D} - \mathcal{B}i\omega)(\mathcal{A}\omega + \mathcal{F}i\omega)}}{\mathcal{D} - \mathcal{B}i\omega}.$$

3.1. Numerical solutions for the full one-dimensional problem. In order to understand the connection between the small amplitude, linear instabilities, and the finite-amplitude, nonlinear steady-state, we solve (2.9), (2.11), and (2.12) numerically. We use a standard second-order finite-difference scheme for spatial derivatives and integrate the equations in time using a Crank–Nicholson method.

The simulations are set up in such a way as to reproduce the experiments that were carried out in [8]. On the experiments, the fluidized bed was excited by a piston located on the entrance of the bed (also working as a distributor) that oscillated with controlled frequency and amplitude. This condition is reproduced numerically by setting the concentration at the entrance as

$$(3.9) \quad \phi_{ent} = \phi_o [1 + \varepsilon \sin(2\pi ft)],$$

where f is the frequency and ε is the amplitude of the oscillations. Given this concentration, the velocity of the particulate phase at the entrance of the bed is given by the condition that the drag and weight corrected for buoyancy balance each other, which gives

$$(3.10) \quad v_{ent} = q - v_t(1 - \phi_{ent})^n.$$

The fluid velocity at the entrance is then calculated using (2.9). The exit condition is obtained by imposing zero second derivatives at the exit, so that the waves can exit the integration domain without affecting the solution. In addition, in order to avoid any kind of contamination originated from possible wave reflections from the exit boundary condition, the boundary was placed very far from the entrance and very far from where the instabilities are expected to reach the finite-amplitude steady-state.

Finally, the initial condition for the simulations is the homogeneous fluidization state, that is, $\phi(x, 0) = \phi_o$, $v(x, 0) = 0$, and $u(x, 0) = q/(1 - \phi_o)$.

4. Closure of the particle phase stress tensor. In order to carry on with the analyses, the constitutive equation for the stress tensor of the particulate phase, (2.4), needs now to be closed, i.e., the particle-phase pressure and the particle-phase viscosity functions need to be known. This is, in fact, the most important pressing problem in the modeling of fluidized beds using the two fluid assumption [8, 9].

4.1. Particle-phase viscosity. In this work, we use the constitutive relation for the particle-phase viscosity that was obtained experimentally in [8]:

$$(4.1) \quad \mu_p(\phi) = 0.18 \frac{\rho_p d_p v_t}{\phi_{rlp} - \phi},$$

with d_p denoting the diameter of the particles, v_t denoting the terminal velocity of the particles, and ϕ_{rlp} denoting a random loose packing concentration, which is not a well defined physical quantity. From the experiments in [8], ϕ_{rlp} was found to be related to the critical concentration ϕ_c (below which the fluidized bed becomes unstable) as

$$(4.2) \quad \phi_{rlp} = \phi_c + 0.025.$$

We note here that since the experiments, as well as the theory that generated the proposal of the constitutive equation for the particle-phase viscosity in [8] were one-dimensional, (4.1) also includes contributions from the second coefficient of viscosity, η_p , that is,

$$(4.3) \quad \mu_p = \frac{4}{3} \mu_p^* + \eta_p,$$

where μ_p^* would denote purely the shear viscosity of the particulate phase.

4.2. Particle-phase pressure. There are also propositions for the particle-phase pressure in [8]. However, the experimental data did not allow the authors to propose one single expression, but rather two, depending on the choice of the density scale. These equations are

$$(4.4) \quad \frac{dp_p}{d\phi} = \frac{7}{10} \rho_f v_t^2 \quad \text{or} \quad \frac{dp_p}{d\phi} = \frac{2}{10} \rho_p v_t^2,$$

which indicate a linear dependence of p_p on ϕ .

The constitutive equations presented in (4.4) were obtained in [8] using an inverse problem approach to find the constitutive relations from the experimentally measured wave profiles. Despite the great achievement of measuring the particle-phase pressure experimentally, there is a significant scatter in the data and, because of that, the authors were unable to choose between the two formulas in (4.4).

Unfortunately, it seems that the linear model for the particle-phase pressure, (4.4), has some limitations. For every combination of physical parameters, there is a critical value of the concentration of particles ϕ_c below which the system goes unstable. Above this value, the fluidization is particulate and no instabilities are observed in the flow. The connection of this observation with the linear theory is straightforward: the growth rates should shift from being negative for all modes (stable state) to a state where they are positive for a certain range of modes as the homogeneous concentration decreases below ϕ_c .

In order to investigate this further, we will focus our attention to one particular experiment carried out in [8], their combination 6, for which the physical parameters are as follows:

$$(4.5) \quad \begin{aligned} \rho_f &= 0.997 \pm 0.002 \text{ g/cm}^3, & \mu_f &= 0.9 \pm 0.02 \text{ cP}, & d_p &= 685 \pm 30 \text{ }\mu\text{m}, \\ \rho_p &= 4.08 \pm 0.01 \text{ g/cm}^3, & v_t &= 16.4 \pm 0.40 \text{ cm/s}, & \phi_{mp} &= 0.612 \pm 0.005, \\ \phi_{rlp} &= 0.580 \pm 0.005, & \phi_o &= 0.549 \pm 0.005, & n &= 3.25 \pm 0.04. \end{aligned}$$

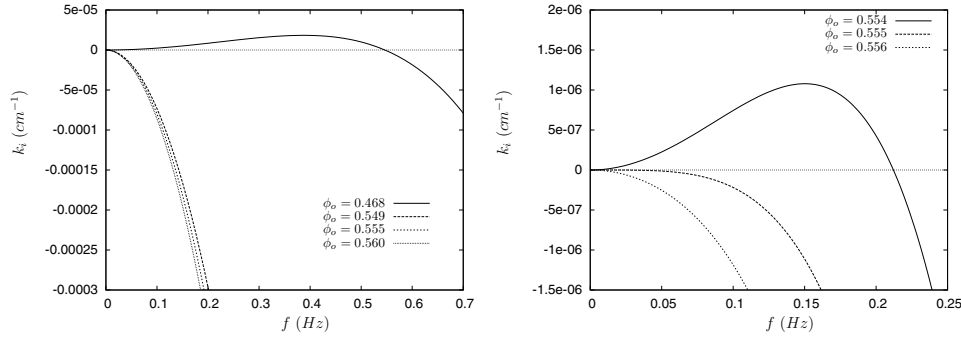


FIG. 1. On the left, growth rates obtained for the physical parameters of this simulation are given in (4.5) and different ϕ_o with $\frac{dp_p}{d\phi} = 187.71$ (cgs). On the right, similar results for $\frac{dp_p}{d\phi} = 131.04$ (cgs).

Taking as reference the set of parameters in (4.5), the values of the particle-phase pressure predicted by (4.4) are

$$(4.6) \quad \frac{dp_p}{d\phi} = \frac{7}{10} \rho_f v_t^2 = 187.71 \text{ (cgs)} \quad \text{or} \quad \frac{dp_p}{d\phi} = \frac{2}{10} \rho_p v_t^2 = 219.47 \text{ (cgs)},$$

where cgs stands for the units of pressure in the centimetre-gram-second system of units. From (4.5), we have that $\phi_c = 0.555$. We choose to set the particle-phase pressure using the smaller value in (4.6) and plot the spatial growth rates in Figure 1 as predicted by (3.8). We observe that for $\frac{dp_p}{d\phi} = 187.71$ (cgs), all the modes are stable down to the very dilute homogeneous concentration of $\phi_o = 0.482 \pm 0.001$. This means that any configuration with $\phi_o \geq 0.483$ is stable. Therefore, simulations launched with particle-phase pressure given by (4.4) and $\phi_o > 0.483$ will generate no results, since any excitation will be decay during the linear phase of its evolution. The larger value in (4.6) would decrease even further the value of the actual ϕ_c for this set of parameters. The right plot in Figure 1 shows that the transition from a stable to an unstable state at $\phi_o = 0.555$ occurs if $\frac{dp_p}{d\phi} \approx 131.04$ (cgs). Therefore, in order to try to recover the experimental results using a linear model similar to (4.6), the model for the particle-phase pressure would have to be

$$(4.7) \quad \frac{dp_p}{d\phi} = 131.04 \text{ (cgs)} \approx \frac{1}{2} \rho_f v_t^2.$$

However, with this model, the system with parameters such as those in (4.5) and $\phi_o = 0.549$ will be stable for all disturbances such that $f > 0.56$ Hz. Therefore, the experimental results obtained in [8] would not be achievable in these simulations.

A vast range of unexpected behavior was obtained from the simulations when the linear particle-phase pressure model was used. If we use the very high values of particle-phase pressure given by (4.6) and (4.7), the small amplitude linearly stable modes do not evolve to a nonlinear state. If we start with larger amplitudes, the results are not too different. If we use smaller values of particle-phase pressure, the simulations collapsed before reaching a steady-state with very large amplitudes and maximum concentrations near to $\phi = \phi_{rlp} = 0.58$. Finally, other phenomena such as period doubling could be observed with this linear particle-phase pressure model, especially when low frequencies and low particle-phase pressures were combined.

A careful examination of the data used in [8] to derive the model in (4.4) gives a hint that the linear model for the particle-phase pressure is not adequate. In fact,

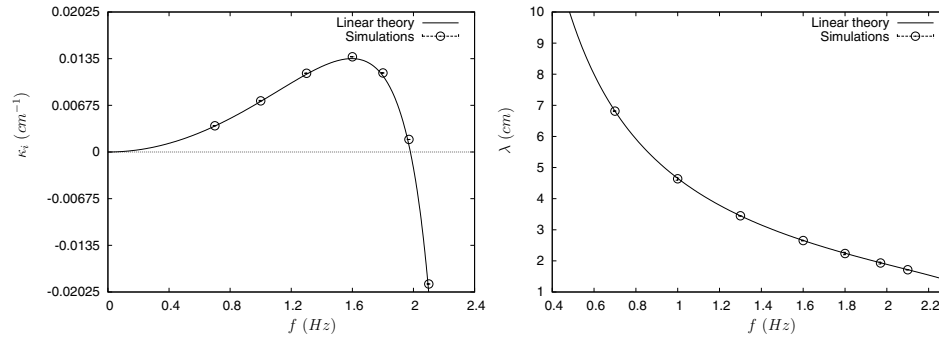


FIG. 2. Validation of the code for very small amplitude spatially evolving waves: spatial growth rates κ_i (left) and wavelength λ (right) of the waves. Results obtained for the parameters as in (4.5).

there is a considerable variation of p_p with $\phi - \phi_o$, most importantly for those points for positive $\phi - \phi_o$. This is an indication that there should be a dependence of $\frac{dp_p}{d\phi}$ on $\phi - \phi_o$. Furthermore, different combinations in [8] presented different dependence with respect on $\phi - \phi_o$.

Therefore, we have opted to use a particle-phase pressure model that is available in the literature that seems to have the right functional behavior with respect to ϕ . We have chosen the ad-hoc model used by [3], given by

$$(4.8) \quad p_p(\phi) = \sigma \phi^3 \exp\left(\frac{r\phi}{\phi_{mp} - \phi}\right),$$

where ϕ_{mp} is the maximum packing concentration and σ and r are constants that should be carefully chosen in order to respect the experimental data regarding the critical concentration for each set of parameters. The values used in this work were $\phi_{mp} = 0.64$, $\sigma = 0.667$, and $r = 0.3$. Other values of these parameters, and the limitations of this model, will be investigated in section 5.

5. Evolution of concentration waves toward saturation. The code developed here was validated by taking very small amplitude waves and tracking their growth along the fluidized bed and comparing their growth rates and wavelengths with respect to those predicted by the linear stability theory. The result can be seen in Figure 2.

The evolution of small amplitude waves toward saturation can be seen in Figure 3. The excitation imposed at the entrance of the bed has a very small amplitude, $\varepsilon_1 = 10^{-4}$, and the frequency is $f = 1.6\text{Hz}$. Superimposed on the profiles, we plot the value of the amplitudes of the waves. It is clear that, as the waves propagate, the amplitude grows and saturates to a well defined value, reaching a steady-state.

The striking feature of the evolution of the waves toward a steady state is the fact that the linear stability theory predicts the growth of the waves correctly up to amplitudes corresponding to $\phi_{\max} - \phi_{\min} \approx 0.01$. After that, when the amplitude of the waves has grown to a significant value for the nonlinear effects to become important, the saturation process starts to occur, resulting in a slower growth rate that eventually becomes zero when the saturation amplitude is reached.

We conclude, therefore, that the theoretical and analytical results of linear stability analysis can be used much further than initially thought. This can be helpful when we address the stability of two-dimensional disturbances, as in [10, 13], where

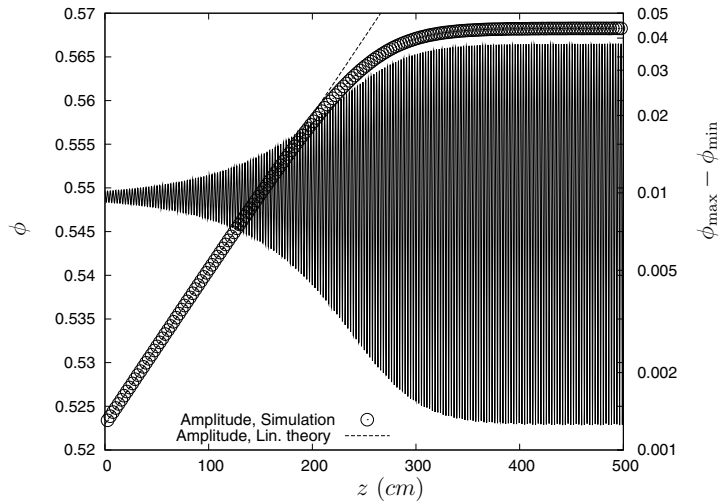


FIG. 3. Evolution of the disturbances towards a saturated state. The particle concentration is plotted with a heavy line, and the amplitude of the waves is plotted with circles. The linear theory prediction is plotted with dashed lines. Results plotted at $t = 724.5s$, obtained for $f = 1.6Hz$ and $\varepsilon_1 = 10^{-4}$. The time step was $\Delta t = 2 \cdot 10^{-4}s$, space step was $\Delta z = 4 \cdot 10^{-2}cm$.

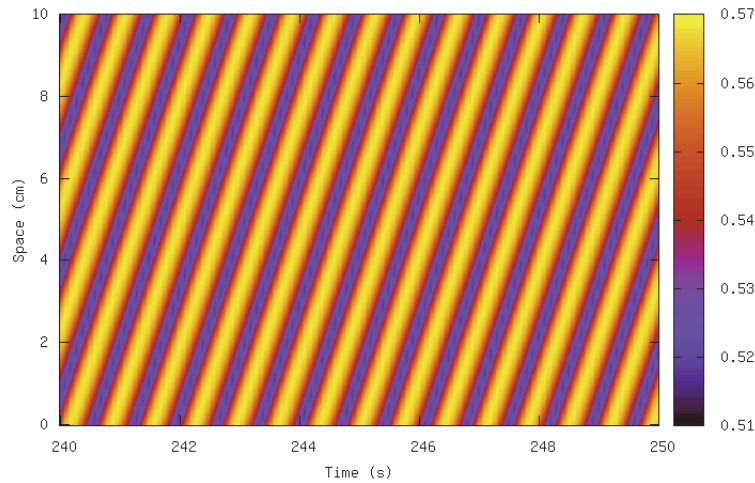


FIG. 4. Spatio-temporal plot of the steady-state waves for the simulation in Figure 3. The space value 0 corresponds roughly to $z = 400cm$.

a more evolved (linear) state needs to be set up as the initial condition of numerical simulations.

The spatio-temporal diagram for the waves at approximately 400cm from the distributor, for the same simulation as in Figure 3, is presented in Figure 4. It shows that a steady-state is actually achieved: crests and troughs of the concentration waves propagate at constant velocity of roughly $c \approx 4.3$ cm/s toward the right.

We now analyze the properties of the steady-state wave profiles obtained in the simulations and the influence of the two most important control parameters of the spatial analysis set up: the excitation frequency and the concentration of particles

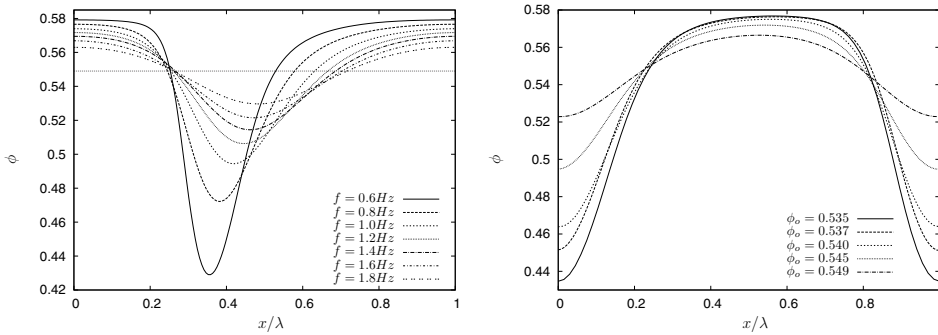


FIG. 5. *Left. The influence of the frequency of excitation on the shape of the saturated waves. The horizontal dashed line indicates the homogeneous value $\phi_o = 0.549$. Right. The influence of the homogeneous concentration on the shape of the saturated waves. Results obtained for 1.6 Hz. Results obtained for the parameters as in (4.5) and plotted against a normalized wavelength.*

at homogeneous fluidization. Note that the saturated state is solely defined by the physical parameters of the system and the frequency of excitation and does not depend on the value of ε .

The form of the saturated wave profiles changes significantly with the frequency of excitation, as can be observed on the left plot in Figure 5. Lower frequency modes are more asymmetric and have much larger amplitudes. On the other hand, high frequency modes exhibit small amplitudes and nearly no asymmetry on the wave profile. Note the asymmetry of the thin region of lower concentrations and the wide region of large concentrations. This is in total agreement with the experimental results in [8] and the numerical results obtained in [3, 6] for different constitutive models.

In fact, the asymmetry of the wave profiles can be understood from the linear stability analysis. The absence of inertia and particle-phase pressure in the model implies that modes have no growth rates, that is, they only propagate up the bed with velocity given by (3.7). Therefore, neutral modes are modes in which inertial and particle-phase pressure mechanisms balance perfectly. The dispersion relation curves presented in Figure 2 show that as the frequency of the disturbances increases, there will be a frequency with zero growth rate and, therefore, modes with frequencies close to that have smaller imbalances of inertia and particle-phase pressure and smaller amplitudes, tending toward a symmetric profile and toward the amplitude of the excitation in the limit of the neutral growth frequency.

The influence of the homogeneous concentration can be seen on the right plot in Figure 5. For the same excitation frequency, in more concentrated fluidized beds, the waves tend to have smaller amplitudes and less asymmetries. The general trend can be observed in Figure 6, where not only the amplitude but also the wavelength of the disturbances is plotted against the homogeneous concentration. From the expression used for the particle-phase pressure p_p in (4.8), we observe that higher concentration beds will have higher levels of particle-phase pressure and, for that reason, the imbalance with the inertial term will be smaller. It is surprising to see that the wavelength of the disturbances is not very sensitive to ϕ_o , although, at a very low concentration, many unforced disturbances are excited and contaminate the finite-amplitude steady-state of the forced mode. The measurements presented in Figure 6 were obtained by averaging over an interval of several wavelengths. Because of these unforced modes, both the wavelength and the amplitude of the forced disturbances

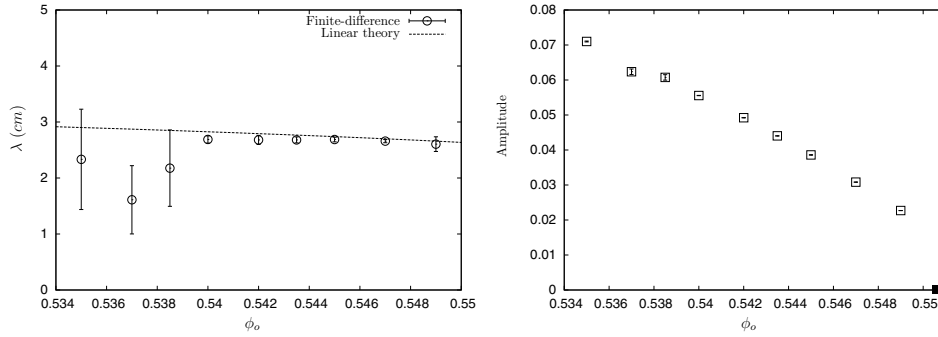


FIG. 6. Comparison of the wavelengths (left) and amplitudes (right) of the saturated waves obtained for different concentration of particles at the homogeneous state, ϕ_0 . The results were obtained for $f = 1.6\text{Hz}$ and with physical parameters given in (4.5). The black square on the right picture identifies the linear theory limit of zero amplitude neutral mode.

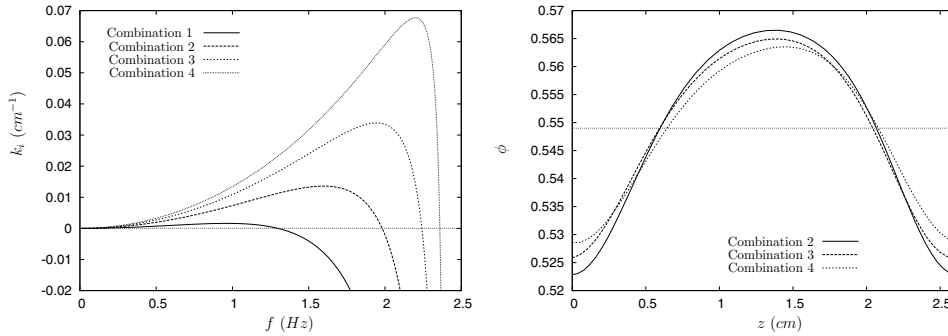


FIG. 7. Left. Growth rates for small amplitude disturbances. Right. Saturated waves profiles. Note that combination 1 in (5.1) and a frequency of 1.6Hz produces a stable mode. The horizontal dashed line indicates the homogeneous value ϕ_0 . Results on both plots were obtained with physical parameters as (4.5), with particle-phase pressure given by (4.8) and with coefficients as in (5.1).

oscillate over this long interval. The error-bars indicate the amount of fluctuation observed on these measurements.

The choice of (4.8) as the particle-phase pressure model used throughout this work was based on previous studies, for example, [3], where it was shown that it reproduces qualitatively the behavior of the dynamics of fluidized beds, and is supported by the lack of more consistent models. The choice of the constants \mathcal{P} and r appearing in the model has to be made carefully, in order to respect the critical concentration for the onset of instabilities. However, this choice is not unique, and herein lies a major limitation of the exponential model of (4.8).

Four possible combinations of parameters that respect the experimental critical concentration for the onset of instabilities for the set of parameters in (4.5) are shown below:

$$(5.1) \quad \begin{array}{ll} \text{Comb. 1: } \mathcal{P} = 51.766, & r = 0.03; \\ \text{Comb. 2: } \mathcal{P} = 0.667, & r = 0.3; \\ \text{Comb. 3: } \mathcal{P} = 0.01879, & r = 0.6; \\ \text{Comb. 4: } \mathcal{P} = 0.0006853, & r = 0.9. \end{array}$$

Using the combinations of parameters in (5.1), the dispersion relations and the saturated wave profiles could be obtained and are shown in Figure 7. The dispersion relations show that the behavior of the modes is significantly altered by the changes

of particle-phase pressure. For instance, modes of frequency $f = 1.6Hz$ can either be stable or unstable, with growth rates varying roughly by a factor of 3. Looking at the saturated wave profiles in Figure 7, not only does the shape of the waves change, but also its amplitude, with variations in $\phi_{\max} - \phi_{\min}$ that can be as large as 0.01. On the other hand, as expected, the particle-phase pressure did not affect at all the wavelength of the saturated waves shown in Figure 7.

Unfortunately, since a reliable and consistent model for particle-phase pressure has not been obtained, either experimentally or theoretically, most of the results in this work have a strong qualitative character but might lack in some quantitative comparisons with experiments. Therefore, discrepancies of the simulation results with the experimental data must be related to the particle-phase pressure and, more generally, with the uncertainties in all the closure models used in the two-fluid formulation.

6. Saturated waves theory. Experimental observations have shown that one-dimensional concentration waves grow in liquid fluidized beds and reach a steady state: they propagate at constant velocity with unchanged form and amplitude. This state is generally referred to as a saturated wave, and we were able to reproduce it in the previous section. Based on these observations, a saturated wave theory that describes such a finite-amplitude steady-state regime can be derived. This was first presented in [8] and, in fact, was their major tool to obtain the constitutive relations presented in (4.1) and (4.4).

The basic assumption of this saturated wave theory is that the waves propagate with constant velocity c up the fluidized bed. Therefore, they are stationary in the frame of reference moving with this velocity, defined by the transformation $Z = x - ct$. The velocities of the fluid and of the particulate phases in this frame of reference are written as, respectively, $u(Z) = u(x, t) - c$ and $v(Z) = v(x, t) - c$, and the particle concentration is now $\phi(Z) = \phi(x, t)$. The one-dimensional continuity equation for the particulate phase and the fluid phase written on the new variables are, respectively,

$$(6.1) \quad -u \frac{d\phi}{dZ} + (1 - \phi) \frac{du}{dZ} = 0 \quad \text{and} \quad v \frac{d\phi}{dZ} + \phi \frac{dv}{dZ} = 0.$$

A direct integration of the second equation in (6.1) gives that $v = -c\phi_o/\phi$, so that, together with (2.9), the velocity of the fluid phase is given by

$$(6.2) \quad u = \frac{q - c\phi_o}{1 - \phi}.$$

One can then eliminate u and v from the momentum equation of the particulate phase in (2.11), written on the new variables, to obtain the following equation in terms of particle concentration only:

$$(6.3) \quad \frac{4}{3}c\phi_o \frac{d}{dZ} \left[\frac{\mu_p(\phi)}{\phi^2} \frac{d\phi}{dZ} \right] + \left[F_2(\phi) - \frac{dp_p}{d\phi} \right] \frac{d\phi}{dZ} + F_1(\phi) = 0.$$

In this equation,

$$(6.4) \quad F_1(\phi) = \phi g(\rho_p - \rho_f) \left[\frac{v_t(1 - \phi_o)^n - c(1 - \phi_o/\phi)}{v_t(1 - \phi)^n} - 1 \right]$$

represents the drag (first term) and the weight corrected for buoyancy (second term), and

$$(6.5) \quad F_2(\phi) = \frac{\phi\rho_f(1 + \vartheta(\phi))}{(1 - \phi)^3} [v_t(1 - \phi_o)^n - c(1 - \phi_o)]^2 + (\rho_p + \vartheta(\phi)\rho_f) \left(\frac{c\phi_o}{\phi} \right)^2$$

represents the inertia of the fluid phase (first term) and that of the particulate phase (second term). Similarly to that observed in the linear case, the dynamics of the saturated waves is mostly determined by the balance between viscous effects, the first term in (6.3), drag and weight corrected for buoyancy, the third term in (6.3), with the inertial and particle pressure contributions, the second term in (6.3), being small corrections.

The boundary conditions for (6.3) are that the solution has to have the minima (or maxima) of the concentration of particles on the extremities of one wavelength, that is,

$$(6.6) \quad \frac{d\phi}{dZ} = 0 \text{ at } Z = 0 \text{ and } Z = \lambda,$$

where $\lambda = 2\pi\kappa^{-1}$ is the wavelength of the disturbances.

6.1. An approximate analytic solution. An approximate analytical solution for the steady-state finite-amplitude waves was derived in [14]. This was achieved by performing further simplifications on (6.3). The first simplification is to neglect the inertial and particle-phase pressure effects and to linearize $F_1(\phi)$ around the homogeneous state. Using the constitutive law for the particle-phase viscosity in (4.1), (6.3) is now written as

$$(6.7) \quad \frac{d}{dZ} \left[\frac{1}{(\phi_{rlp} - \phi)} \frac{d\phi}{dZ} \right] + \mathcal{G}(\phi - \phi_o) = 0,$$

assuming that $1/\phi^2 \approx 1/\phi_o^2$ inside the outer derivative on the right-hand side of (6.3), and with

$$(6.8) \quad \mathcal{G} = \frac{c_o - nc}{cl^2(\phi_{rlp} - \phi_o)}.$$

Now, defining the change of variables $\Psi = -\ln(\phi_{rlp} - \phi)$, (6.7) becomes

$$(6.9) \quad \frac{d^2\Psi}{dZ^2} + \mathcal{G}(e^{-\Psi_o} - e^{-\Psi}) = 0,$$

where Ψ_o stands for $\Psi(\phi_o)$. Multiplying (6.9) by $d\Psi/dZ$ and integrating once with respect to Z , we get

$$(6.10) \quad \left(\frac{d\Psi}{dZ} \right)^2 + 2\mathcal{G}\Psi e^{-\Psi_o} + 2\mathcal{G}e^{-\Psi} = \text{constant} = 2\mathcal{G}\Psi_{\max} e^{-\Psi_o} + 2\mathcal{G}e^{-\Psi_{\max}},$$

the constant being found by the condition of zero derivative at the maximum concentration of the wave profile. For large amplitude waves, near the maximum region, $\Psi \approx \Psi_{\max}$ and (6.10) can be further simplified to

$$(6.11) \quad \left(\frac{d\Psi}{dZ} \right)^2 + 2\mathcal{G}(\Psi_{\max} - \Psi)e^{-\Psi_o} = 0.$$

Finally, integrating this equation and returning to the variable ϕ , we obtain

$$(6.12) \quad \phi = \phi_{rlp} - (\phi_{rlp} - \phi_{\max}) e^{\frac{\mathcal{G}}{2}(\phi_{rlp} - \phi_o)Z^2}.$$

In addition to (6.12) found in [8], we used the same arguments to find an approximation for ϕ near the minimum concentration regions:

$$(6.13) \quad \phi = \phi_{rlp} - (\phi_{rlp} - \phi_{\min}) \left[\cosh \left(\frac{\mathcal{G}(\phi_{rlp} - \phi_{\min})}{4} Z \right) \right]^{-2}.$$

Furthermore, a relationship between the maximum and the minimum concentrations can be obtained from (6.10), that is

$$(6.14) \quad (\Psi_{\min} - \Psi_{\max}) e^{-\Psi_o} + e^{-\Psi_{\min}} - e^{-\Psi_{\max}} = 0.$$

It should be noted that the velocity of propagation of the waves was assumed to be known in this derivation. It is also observed that (6.12) does not provide an oscillatory profile, therefore being unable to determine the wavelength of the disturbances.

6.2. Numerical solutions of the saturated regime equations. The main difficulty in finding a solution to (6.3) is that it is an eigenvalue problem, i.e., both the concentration profile and the velocity of propagation of the waves have to be determined as a solution of the problem. Therefore, in addition to (6.3) and its boundary condition, another equation is necessary.

Multiplying (6.3) by $\mu_p(\phi)/\phi^2 \times \frac{d\phi}{dZ}$ and integrating the resulting equation over one wavelength, taking into account the boundary condition in (6.6) and the condition for periodicity, the following integral restriction can be obtained:

$$(6.15) \quad \int_0^\lambda \mu_p(\phi) \left[F_2(\phi) - \frac{dp_p}{d\phi} \right] \left(\frac{1}{\phi} \frac{d\phi}{dZ} \right)^2 dZ = 0.$$

Now, (6.15), together with (6.3) and (6.6), form a system that can be solved numerically for both $\phi(Z)$ and c .

The process implemented to find a solution of (6.3), (6.6), and (6.15) is the following: for a given set of the physical parameters, an arbitrary value of the propagation velocity is chosen in the interval $(0, c_o)$. Using this value of c , (6.3) is integrated via a Runge–Kutta scheme of fourth order, starting from the initial state of minimum concentration ϕ_{\min} at $Z = 0$. The integration is performed until the next minimum of the concentration of particles is found, that is, after one wavelength λ is integrated. However, since c might not be the correct value, the minimum found does not necessarily have the same value as the initial input value at $Z = 0$, and we would have not found a steady-state profile. This integral constraint in (6.15) is a better test to verify that the wave obtained actually corresponds to the steady-state finite-amplitude we are looking for. This integral is evaluated numerically by a Simpson rule. The profile obtained via the Runge–Kutta integration is used to check the integral restriction: if (6.15) is not satisfied, then another guess for c must be tried. A bisection method is used to find c iteratively in order to satisfy (6.15). Finally, in order to find the wave profile for a given frequency f , another bisection method was coupled to the method described above to find the correct ϕ_{\min} necessary to have the desired f . Therefore, the solution of (6.3), (6.6), and (6.15) by this method provides not only the wave profile and the wavelength λ of the disturbances but also their propagation velocity c .

6.3. Concentration profiles in the saturated regime. Figure 8 shows a wave profile found using the method described in the previous section. It is observed that the concentration waves have a flat wide top, where viscous effects dominate the shape of the wave, as opposed to the less viscous narrow regions around the minima,

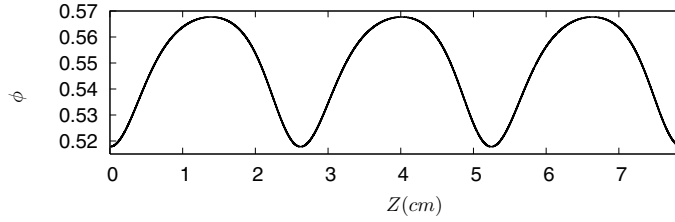


FIG. 8. Saturated wave profiles obtained for the configuration presented in (4.5) with $\phi_o = 0.549$ and $f = 1.6\text{Hz}$. Three wave-lengths were plotted in this graph.

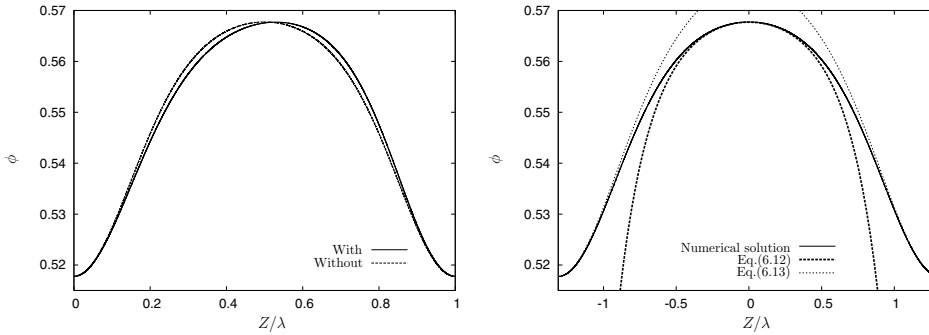


FIG. 9. Left. Comparison of the saturated wave profiles obtained numerically with and without the inertia and particle-phase pressure terms in (6.3), for $f = 1.6\text{Hz}$. Right. Comparison of the saturated wave profiles obtained numerically, without inertia and particle-phase pressure terms in (6.3), and via the approximate analytical solutions given by (6.12) and (6.13), for $c = 4.19581289\text{ cm/s}$, $\phi_{\min} = 0.51779590$ and $\phi_{\max} = 0.56770461$ from the numerical solution. In both plots, $\phi_o = 0.549$ and all other parameters as in (4.5).

where drag and weight correct for buoyancy dominate. In addition, one observes a subtle asymmetry of the wave profile, caused by the inertia of the flow. We note here that these general trends are in agreement with the experimental observations of [8]. The propagation velocity of these waves was found to be $c = 4.322\text{ cm/s}$, similar to the one calculated in Figure 4.

Due to the fact that the waves presented in Figure 8 are plotted in a modified spatial coordinate, as opposed to a temporal coordinate, the asymmetry of the waves observed in Figure 8 is the opposite to that observed in the experimental data obtained in [8], but similar to that obtained in [3]. In fact, as discussed in [4], this apparent inconsistency comes from the assumption of the particle-phase pressure model (4.8): the particle-phase pressure might not grow without bounds as $\phi \rightarrow \phi_{mp}$, as discussed in [2], or maybe it does, but with a different functional behavior, that can even be different when in the compression or in the expansion phases of a concentration wave, as recently suggested in [7]. All these might be crucial to reproduce the experimental asymmetry of the waves.

If one neglects the inertial and particle-phase pressure terms in (6.3), a symmetrical profile is obtained, as can be seen on the left picture in Figure 9. Note that inertia and particle-phase pressure terms are only neglected in (6.3), that is, the calculation of the profile still needs to satisfy (6.15). The propagation velocity and the wavelength of the wave are almost unaffected by that simplification, as already suggested by the linearized studies when inertia is neglected.

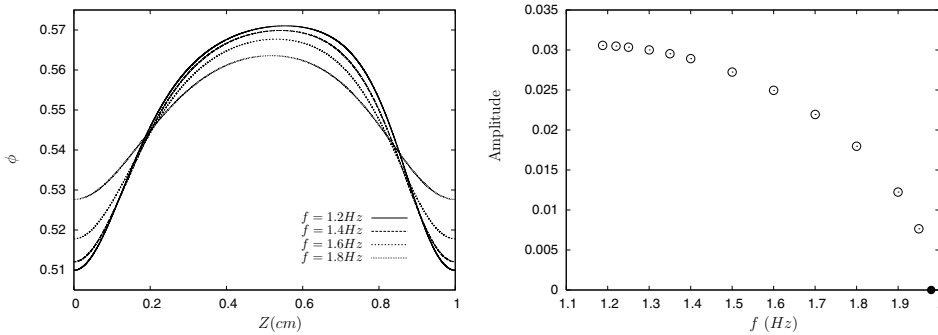


FIG. 10. *Left. Comparison of the saturated wave profiles obtained for different frequencies. Right. Amplitudes of the waves as a function of the frequency. The black circle identifies the linear theory limit of zero amplitude. In both plots, $\phi_o = 0.549$ and all other parameters as in (4.5).*

The comparison of the results obtained from the numerical solution with the approximate analytical solution obtained in (6.12) is presented on the right picture in Figure 9. In order to compare the results, the maximum and minimum concentrations and the propagation velocity of the saturated waves have to be given to (6.12) and (6.13). It is seen that the analytical solution in (6.12) can only describe the flat top near the maximum concentration of the wave profiles, whereas the solution in (6.13) can only describe the regions near the minimum concentration. Note that these expressions are being compared with the wave profile obtained without inertia and particle-phase pressure terms in (6.3), since this was part of the simplifications necessary to obtain the analytical solutions. Therefore, (6.12) and (6.13) cannot capture any asymmetry of the wave. In addition, if we assume $\phi_{\max} = 0.56770461$ from the numerical solution, (6.14) predicts $\phi_{\min} = 0.5171059$, very close to the value of $\phi_{\min} = 0.51779590$, calculated from the numerical solution.

The influence of the frequency of the disturbances on the shape of the steady-state profiles is observed in Figure 10, where the amplitude of the waves, defined as $\frac{1}{2}(\phi_{\max} - \phi_{\min})$, is plotted as a function of the frequency of the waves. We observe that the amplitude and the asymmetry of the profiles are reduced as the frequency increases. In fact, the waves show a more sinusoidal profile as their frequency approaches the frequency of neutral growth disturbance predicted from the linear stability, which is $f \approx 1.97 Hz$. We also observe that there is a tendency for waves of low frequency to have similar amplitudes, indicating that there might be a maximum amplitude for a given set of physical parameters. Unfortunately, the simulations could not be pushed further to the low frequency limit, as convergence is not reached, mainly because the integral in (6.15) never reaches zero.

Figure 11 shows the dependence of the propagation velocity and the wavelength of the saturated waves with the frequency of the disturbances and compares the results with the predictions of the linear theory. We observe that the velocity of the high frequency modes are very similar to those predicted by the linear theory. As the frequency decreases and the amplitude (i.e., the non-linearity) of the waves increase, the velocity drifts away from the linear theory, although no more than 5% slower than the linear theory prediction. This is in qualitative agreement with the results obtained in [3], where the variations of the velocity of the saturated waves was not greater than 10%. Therefore, the linear theory predictions of the velocity of propagation of the waves in surprisingly good, even for large amplitude waves.

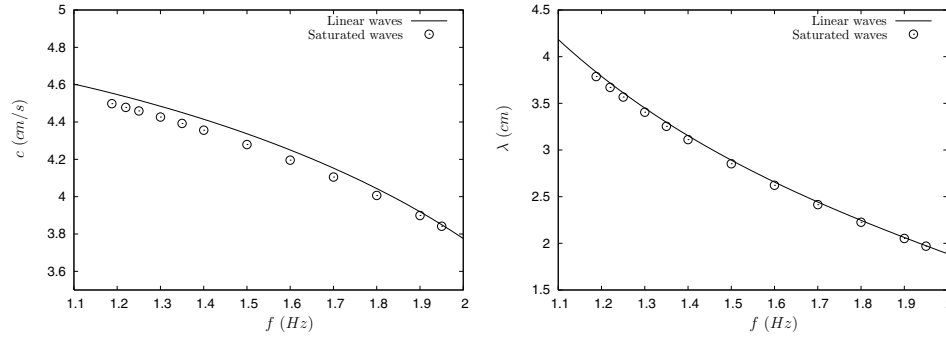


FIG. 11. Propagation velocity (right) and wavelength (right) of the saturated waves as a function of the frequency of the waves. In both plots, $\phi_o = 0.549$ and all other parameters are as in (4.5).

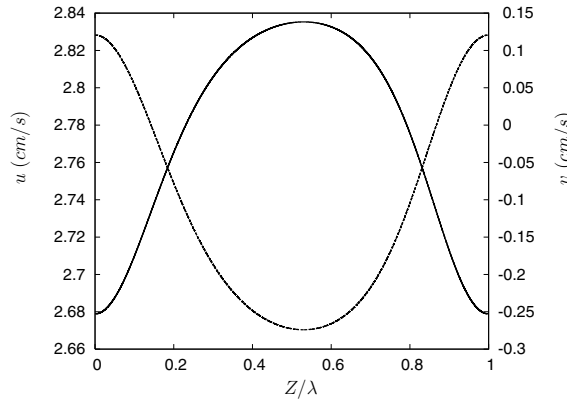


FIG. 12. Velocity profiles obtained for the configuration presented in (4.5) with $\phi_o = 0.549$. The propagation velocity of this wave is approximately $c = 4.2\text{cm/s}$, and its frequency is $f = 1.6\text{Hz}$. The continuous line denotes the particulate phase velocity, in phase with the concentration profile presented in Figure 8, and the dashed lines represent the out-of-phase fluid phase velocity.

Finally, Figure 12 gives the velocities of the fluid and particulate phases as seen in the laboratory frame for the concentration wave shown in Figure 8. It is observed that the particulate-phase velocity is in phase with the concentration profile, whereas the fluid-phase is out of phase by π . The fluid phase velocity oscillates around the value $q/(1 - \phi_o)$, that is, the velocity of the fluid in the homogeneous fluidization state. The particulate-phase velocity, however, oscillates around zero. This indicates that higher concentration regions travel upward and the lower concentration regions downward. This is associated with the mechanism of propagation of the concentration waves in fluidized beds, where the particles from the lower surface of a wave fall toward the front of the next wave (usually referred to as “rain of particles”), as widely described in the observations in the literature, for example, [8].

7. Comparisons of the two methods. We shall now compare the results obtained for the full theory from the finite-difference simulations and the saturated wave theory for the saturated waves. We will also attempt to make some comparisons with the experimental data available in [8] for the set of parameters presented in (4.5).

A comparison of the profiles obtained from the two different methods is presented on the left plot in Figure 13. It is observed that the matching of the profiles is not

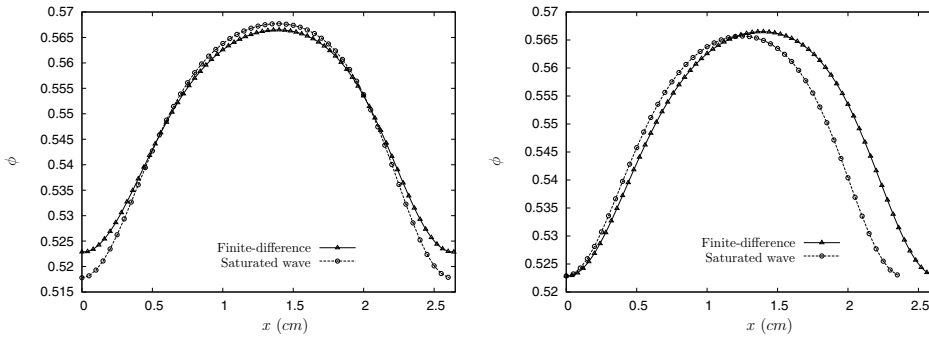


FIG. 13. Comparisons of the steady-state concentration profiles obtained via the unsteady finite-differences simulations and via the saturated wave theory. On the left plot, both profiles were calculated for $f = 1.6\text{Hz}$. On the right plot, both profiles were calculated for the same $\phi_{\min} = 0.52287$. On both plots, physical parameters are given in (4.5).

perfect, even though they were meant to be the results of a finite-amplitude steady-state wave profile for a same set of physical parameters of the system. Although the result from the unsteady finite-differences simulations has a remarkably similar asymmetry and virtually the same wavelength as that by the saturated wave theory, it has a considerably smaller amplitude. The wavelength found via the finite-difference method is $\lambda = 2.6047\text{cm}$, whereas that found via the saturated wave theory is $\lambda = 2.6224\text{cm}$. Note that this small difference is of the order of the discretization accuracy. The amplitude found via the finite-difference method is 0.0454, whereas that found via the saturated wave theory is 0.0499, that is, around 10% larger.

If we set the minimum concentration for the calculation of the saturated wave theory equal to the one obtained on the finite-difference calculation, the profile obtained is presented on the right plot in Figure 13. We observe that now the agreement of the amplitudes is better, with the saturated wave theory predicting 0.0428, about 5% smaller than the one obtained by the finite-difference method. However, the wavelength is about 10% shorter and the frequency of the new wave is $f = 1.715\text{Hz}$.

As observed in the literature [8], a broad spectrum of unforced higher harmonics can be excited and propagate in experiments and also on the solution of (2.9), (2.11), and (2.12). Therefore, the different nonlinear interactions in the finite-difference simulations do not lead to profiles that are not purely of the desired forced frequency, as the solution obtained via (6.3) does. The fact that the wave profile obtained from the unsteady finite-differences simulations has a smaller amplitude than the mode with the same frequency calculated by the saturated wave theory in Figure 13, characteristic of high frequency waves, and that a better agreement in the amplitude of the waves is achieved for waves of higher frequencies in the saturated wave theory, corroborate this idea. In addition, as the problem lies in the amplitude of the waves, the uncertainty in the particle-phase pressure and the way that it interacts nonlinearly with other modes might also play a role in the differences observed in Figure 13.

Figure 14 shows the wavelength and the amplitude of the finite-amplitude steady-state wave profile, obtained with the unsteady finite-differences simulations and with the saturated wave theory, with respect to the frequency of the waves. These results are also compared with the experimental data available in [8]. The wavelength of the disturbances is very well captured by both methods and is in very good agreement with the experiments and, surprisingly, with the linear theory, for most of the range of

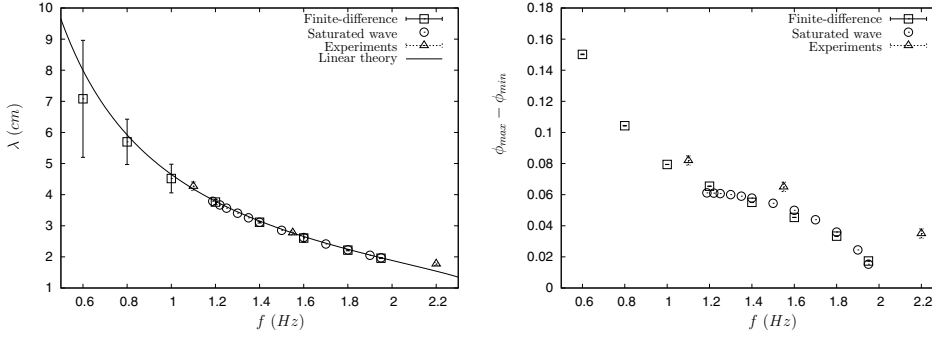


FIG. 14. Comparison of the wavelengths (left) and amplitudes (right) of the saturated waves obtained using via the unsteady finite-differences simulations and via the saturated wave theory with the experimental results available in [8]. The physical parameters given in (4.5).

frequencies investigated here. This shows that the wavelength of the waves does not change as they grow from small linear disturbances to a finite-amplitude nonlinear steady-state.

In the low frequency limit, the presence of unavoidable higher harmonics in the flow leads to an underestimation of the wavelength. On the other hand, the higher frequencies limit is more subtle. The linear stability analysis results in Figure 2 show that that frequencies higher than approximately $2Hz$ have negative spatial growth rates and cannot be excited, grow, and reach the finite-amplitude steady-state in a fluidized bed for this set of parameters. Therefore, it is not possible to generate these modes in the simulations. The existence of a finite-amplitude steady-state with $f = 2.2Hz$ in the experiments indicates that the model for the particle-phase pressure is not providing an accurate cut-off of the frequencies.

Despite the amplitudes obtained with the two different methodologies in Figure 14 agree within 10%, they do not agree with the experimental results, for the reasons mentioned previously in this section. It seems that the trend of the dependence of the amplitudes on the frequency is well captured at the moderate frequencies, even though more experimental points would be necessary to confirm this. Moreover, the absence of experimental points for the lower frequencies, as well as the inability of the saturated wave theory to determine the wave profiles at very low frequencies, restrict our analysis on the behavior of the amplitudes in this regime. Similar remarks hold for the results presented in Figure 15, where the maximum and minimum concentrations of the finite-amplitude steady-state waves are presented. It is observed, however, that the disagreement of the maximum concentrations is more pronounced than that of the minimum concentration. Therefore, one may conclude that not only the uncertainties in the particle-phase pressure, responsible for setting the asymmetry and the minimum concentration of the waves, but also in the particle-phase viscosity (uncertainty specially critical in the definition of ϕ_{rp} [8]) are linked to the behavior observed here.

8. Final remarks. In this work we have investigated the behavior of one-dimensional instabilities in fluidized beds, from the range of very small amplitudes to finite amplitude steady states. We observed that the linear theory can be used to predict correctly the growth of the waves not only for small amplitudes, but also up to moderate amplitudes. Saturated waves were obtained as the solution of an eigenvalue problem, composed of an ordinary differential equation and an integral restriction, and there is a very good agreement with the waves obtained as the result

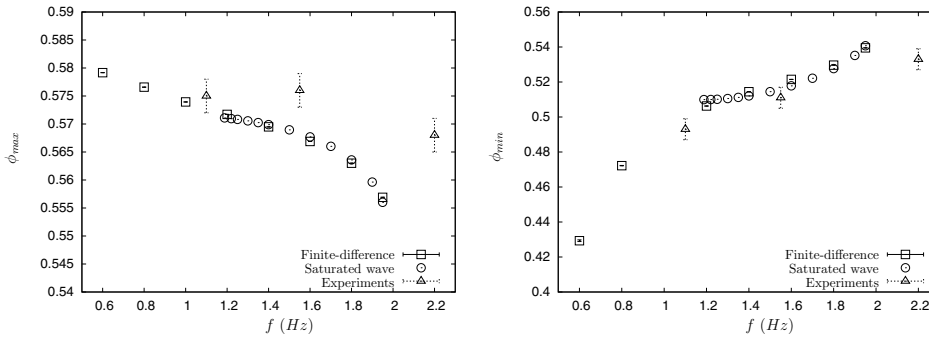


FIG. 15. Comparison of the maximum (left) and minimum (right) concentration of particles obtained for the saturated waves using the unsteady finite-differences simulations and the saturated wave theory with the experimental results available in [8]. The physical parameters given in (4.5).

of the evolution of small amplitude disturbances. The concentration profiles obtained in saturated regime are unique for each set of parameters and depend significantly on the constitutive models used for the particulate phase properties. Therefore, despite the good qualitative predictions of the two-fluid formulation, quantitative comparisons with experiments still have to be improved. In fact, more experimental and theoretical work has to be devoted to understanding of the closure relations of the two-fluid formulation of fluidized beds.

REFERENCES

- [1] R. JACKSON, *The Dynamics of Fluidised Particles*, Cambridge University Press, Cambridge, 2000.
- [2] S. SUNDARESAN, *Instabilities in fluidized beds*, *Annu. Rev. Fluid Mech.*, 35 (2003), pp. 63–88.
- [3] K. ANDERSON, S. SUNDARESAN, AND R. JACKSON, *Instabilities and the formation of bubbles in fluidized beds*, *J. Fluid Mech.*, 303 (1995), pp. 327–366.
- [4] E. GUAZZELLI, *Fluidized Beds: From Waves to Bubbles*, in *The Physics of Granular Media*, H. Hinrichsen and D. E. Wolf, eds., Wiley-VCH Verlag, Berlin, 2004, pp. 213–237.
- [5] M. F. GÖZ AND S. SUNDARESAN, *The growth, saturation, and scaling behaviour of one- and two-dimensional disturbances in fluidized beds*, *J. Fluid Mech.*, 362 (1998), pp. 83–119.
- [6] B. J. GLASSER, I. G. KEVREKIDIS, AND S. SUNDARESAN, *Fully developed travelling wave solutions and bubble formation in fluidized beds*, *J. Fluid Mech.*, 334 (1997), pp. 157–188.
- [7] J. J. DERKSEN AND S. SUNDARESAN, *Direct numerical simulation of dense suspensions: Wave instabilities in liquid-fluidised beds*, *J. Fluid Mech.*, 587 (2007), pp. 303–336.
- [8] P. DURU, M. NICOLAS, E. J. HINCH, AND E. GUAZZELLI, *Constitutive laws in liquid-fluidized beds*, *J. Fluid Mech.*, 452 (2002), pp. 371–404.
- [9] T. B. ANDERSON AND R. JACKSON, *A fluid mechanical description of fluidized beds: Equations of motion*, *Ind. Eng. Chem. Fundam.*, 6 (1967), pp. 527–539.
- [10] K. MANDICH AND R. J. CATTOLICA, *Longitudinal and transverse disturbances in unbounded gas-fluidized beds*, *Phys. Fluids*, 25 (2013), p. 023301.
- [11] J. F. RICHARDSON AND W. N. ZAKI, *Sedimentation and fluidization*, *Trans. Inst. Chem. Eng.*, 32 (1954), pp. 35–52.
- [12] M. NICOLAS, J.-M. CHOMAZ, AND E. GUAZZELLI, *Absolute and convective instabilities of fluidized beds*, *Phys. Fluids*, 6 (1994), pp. 3936–3944.
- [13] Y. D. SOBRAL AND E. J. HINCH, *Gravitational overturning in stratified particulate flows*, *SIAM J. Appl. Math.*, 71 (2011), pp. 2151–2167.
- [14] P. DURU, *Lois Constitutives et Instabilités en Fluidisation Liquide-Solide*, Ph.D. thesis, Université de Provence, France, 2001.